

Full length article



Self-stabilization of the equilibrium state in ferroelectric thin films

Peter Gaal^{a,b,*}, Daniel Schmidt^{a,b}, Mallika Khosla^a, Carsten Richter^a, Peter Boesecke^c, Dmitri Novikov^d, Martin Schmidbauer^a, Jutta Schwarzkopf^a

^a Leibniz-Institut für Kristallzüchtung, Max-Born-Straße 2, 12489 Berlin, Germany

^b TXproducts UG, Luruper Hauptstrasse 1, 22547 Hamburg, Germany

^c European Synchrotron ESRF, 71, Avenue des Martyrs, Grenoble Cedex 9, 38043, France

^d Deutsches Elektronen-Synchrotron DESY, Notkestraße 85, 22607 Hamburg, Germany

ARTICLE INFO

Dataset link: <https://doi.org/10.1515/ESRF-E-S-594730606>

Keywords:

Electrocalorics
Phase transitions
Piezoelectrics
Time-resolved XRD
Multiferroics

ABSTRACT

(K,Na)NbO₃ is a lead-free and sustainable ferroelectric material with electromechanical parameters comparable to Pb(Zr,Ti)O₃ (PZT) and other lead-based solid solutions. It is therefore a promising candidate for caloric cooling and energy harvesting applications. Specifically, the structural transition from the low-temperature Mc- to the high-temperature c-phase displays a rich hierarchical order of domains and superdomains, that forms at specific strain conditions. The relevant length scales are few tens of nanometers for the domain and few micrometers for the superdomain size, respectively. Phase-field calculations show that this hierarchical order adds to the total free energy of the solid. Thus, domains and their formation has a strong impact on the functional properties relevant for electrocaloric cooling or energy harvesting applications. However, monitoring the formation of domains and superdomains is difficult and requires both, high spatial and high temporal resolution of the experiment. Synchrotron-based time-resolved X-ray diffraction methods in combination with scanning imaging X-ray microscopy is applied to resolve the local dynamics of the domain morphology with sub-micrometer spatial and nanosecond temporal resolution. In this regime, the material displays a novel self-stabilization mechanism of the domain morphology, which may be a general property of first-order phase transitions.

1. Introduction

The formation of domains in ferroelectric (FE) materials has a strong impact on the materials functional properties and was studied in different material systems such as Rochelle Salt [1], Pb(Zr,Ti)O₃ [2,3] or BaTiO₃ [4–7]. In general, domains form in order to minimize the free energy of the system [5,8–10], e.g., through stress relief at the domain wall [11,12]. In thin FE films, the equilibrium domain distribution can be manipulated via the lattice mismatch to the substrate [13], which is often referred to as strain [14]- and domain engineering [15, 16]. The domain morphology, i.e. the spatial distribution of domains, forms as the systems undergoes a phase transition [17,18]. Structural phase transitions are also highly interesting, in particular due to their strong impact on functional properties such as the piezoelectric coefficients [19,20]. Various models for domain growth across a phase transition have been proposed, such as defect domain nucleation [4], polarized cluster precursors [6], multi-step nucleation [21, 22] or avalanche-like propagation of phase fronts [23]. The multitude of proposed models and mechanisms suggests, that a unified picture of domain formation across the phase transition in FEs is still missing.

This holds especially in regard to the stability of a domain distribution across a phase transition. On the one hand, an increase of domain wall fluctuations [7] as well as a reduced pinning of domain walls at crystal defects [24] near the phase transition temperature has been suggested. Both effects favor a randomization of the spatial domain distribution across the phase transition. On the other hand, a number of groups reported the stabilization of a spatial domain pattern across a phase transition [25–28]. As a trend, domain distributions are more stable upon cooling than heating [27]. Ab-initio calculations show that the stability of domain walls across a phase transition depends on their orientation [28], a result that has been predicted [29] and experimentally observed [26] earlier. Density-Functional theory suggests that a domain morphology which is stable across the phase transition is energetically favorable [30]. However, experimental studies are challenging because high spatial and temporal resolution are necessary simultaneously to resolve the spatiotemporal evolution of a domain pattern. The necessary techniques, such as time-resolved transmission electron [31] or X-ray [32] microscopy are becoming available just now.

* Corresponding author at: Leibniz-Institut für Kristallzüchtung, Max-Born-Straße 2, 12489 Berlin, Germany.
E-mail address: peter.gaal@ikz-berlin.de (P. Gaal).

<https://doi.org/10.1016/j.apsusc.2022.155891>

Received 30 September 2022; Received in revised form 24 November 2022; Accepted 26 November 2022

Available online 29 November 2022

0169-4332/© 2022 The Authors. Published by Elsevier B.V. This is an open access article under the CC BY license (<http://creativecommons.org/licenses/by/4.0/>).

In this work, we investigate the spatiotemporal formation of hierarchical domains across a first order structural phase transition with nanosecond temporal and sub- μm spatial resolution. We study thin films of Potassium-Sodium-Niobate ($(\text{K},\text{Na})\text{NbO}_3$), which is regarded as one of the most promising lead-free piezoelectric materials in respect to its electromechanical, electrooptical and thermoelectric properties [33]. We employ nanosecond laser pulses to heat epitaxial $(\text{K},\text{Na})\text{NbO}_3$ thin films across the thermotropic phase boundary [34]. By combining time-resolved reciprocal space mapping (RSM) with scanning diffraction imaging we obtain a time-dependent real-space mapping of short and long range domains and superdomains. The latter denote a hierarchical organization of polydomains [35] which occurs in a number of multiferroic materials [36,37]. As a first result, we quantify the temperature range of the monoclinic-to-orthorhombic phase transition on a nanosecond timescale. As a second result, we demonstrate an energy-dependent self-stabilization of the spatial domain distribution across the thermotropic phase transition. Our results provide a characterization of a structural phase transition on nanosecond timescales relevant for applications such as electrocaloric cooling [38] and energy harvesting [39]

2. Results and discussion

We investigate ferroelectric $\text{K}_x\text{Na}_{1-x}\text{NbO}_3$ strained thin films that undergo a thermally driven first order phase transition from the low-temperature M_c monoclinic phase at room temperature to the orthorhombic c -phase at high temperatures. The M_c and c phases are both ferroelectric [40] and are stabilized by the anisotropic compressive epitaxial strain induced by coherent growth of the thin films on suitable substrates. The phase transition temperature of the corresponding ferro-to-ferroelectric phase transition can be tuned over a large temperature interval by changing the magnitude of the compressive strain [40]. Both phases are connected to a characteristic domain arrangement that exhibits a wide variety of hierarchical ordering phenomena.

We study a particular, albeit representative instance of this material system, namely a 50 nm thin $\text{K}_{0.7}\text{Na}_{0.3}\text{NbO}_3$ film grown on an intermediate 20 nm thin Strontium Ruthenate SrRuO_3 (SRO) electrode, with both layers coherently deposited on top of a TbScO_3 (TSO) substrate. In the following, we summarize the 3D domain morphology and the respective crystallographic orientation of the structure. A detailed discussion was published elsewhere [41].

The (110) surface orientation of the TbScO_3 substrate provides a rectangular surface unit cell at room temperature with nearly identical dimensions of $2 \times 3.953 \text{ \AA}$ and $2 \times 3.957 \text{ \AA}$ along the $[001]_{TSO}$ and $[1\bar{1}0]_{TSO}$ in-plane directions, respectively [42]. This leads to c_{pc} pseudocubic orientation of the $\text{K}_{0.7}\text{Na}_{0.3}\text{NbO}_3$ thin film with corresponding in-plane strains of 0.1% and -1.4% along the a_{pc} and b_{pc} pseudocubic directions, respectively.

The pseudocubic notation [43] is used throughout this work for the $\text{K}_{0.7}\text{Na}_{0.3}\text{NbO}_3$ film, while the TbScO_3 substrate is referenced in orthorhombic notation. Piezoresponse force microscopy (PFM) and X-ray diffraction revealed a hierarchical arrangement of ferroelectric domains and superdomains in the $\text{K}_{0.7}\text{Na}_{0.3}\text{NbO}_3$ film. At room temperature the sample exhibits periodically arranged stripe domains consisting of the monoclinic M_c -phase, as depicted in Fig. 1(b). The monoclinic unit cells of adjacent stripe domains differ by a 90° in-plane rotation. In the ferroelectric M_c -phase the polarization vector is oriented along the face diagonal of the sheared unit cell [cf. Fig. 1(a)]. Four different variants of stripe domain patterns can be observed, distinguished by 0° , 90° , 180° and 270° in-plane orientation of the monoclinic shearing displayed in Fig. 1(a). These superdomains have irregular shape with lateral dimensions on the micrometer length scale, while the stripe domains within each superdomain are very regular and exhibit smooth domain walls with a lateral period of about 45 nm.

The hierarchical domain arrangement observed in the PFM images is also evident in the corresponding X-ray diffraction patterns. Fig. 1(c)

exemplifies the 2D intensity distribution in the vicinity of the out-of-plane (620) TbScO_3 substrate Bragg reflection. It shows a complex satellite pattern caused by the well-ordered ferroelectric M_c domain morphology. From the in-plane spacing of the satellite peaks, Δq_{ds} , we deduce the lateral period of the stripe domains to 45 nm, regardless of the type of superdomain. In addition, we observe two branches of satellite reflections with opposite tilt [indicated by white dashed lines in Fig. 1(c)], which originate in the $0^\circ/90^\circ$ and the $180^\circ/270^\circ$ superdomain variants. The horizontal position of the central peak of the two branches ($q_{\parallel} = 3.157 \text{ \AA}^{-1}$) coincides with the horizontal position of the (620) TbScO_3 substrate Bragg reflection (which occurs at $q_{\perp} = 6.504 \text{ \AA}^{-1}$ and is not shown here) confirming a fully strained film. The two branches show a vertical splitting Δq_{\perp} [indicated by the black arrows in Fig. 1(c)] from which the monoclinic angle between the b_{pc} and c_{pc} axes of the monoclinic unit cell can be determined to $\alpha = 89.9^\circ$.

Upon increasing the film temperature, the intensity of the satellite peaks caused by the periodic stripe domains decreases until they disappear completely at temperatures higher than 100°C [cf. Fig. 1(d)–(e)]. At the same time, the central $\text{K}_{0.7}\text{Na}_{0.3}\text{NbO}_3$ film peak superimposed on the crystal truncation rod at $q_{\parallel} = 3.157 \text{ \AA}^{-1}$ increases in intensity. This is a strong indication of a structural phase transition from the stripe-ordered monoclinic M_c -phase – which can be identified by the satellite peaks – to the orthorhombic c -phase, which does not show a periodic domain pattern and therefore manifests itself in a strong central peak at $q_{\parallel} = 3.157 \text{ \AA}^{-1}$. For the orthorhombic phase we do not observe a vertical peak splitting since the angle between the b_{pc} and c_{pc} axes equals $\alpha = 90^\circ$. During the phase transformation, neither the in-plane spacing of the M_c satellite peaks nor the vertical splitting and orientation (given by the 3D domain wall orientation) of the individual branches change with temperature. We have evaluated the intensity of the M_c satellite peaks and of the central peak across the phase transition. The former is a measure of the volume fraction of the M_c phase while the latter depends on the volume fraction of the c phase. Upon increasing the temperature the diffracted intensity from the M_c phase is gradually reduced, while the diffraction from c -phase simultaneously increases [cf. Fig. 1(f)]. The total diffracted intensity from the $\text{K}_{0.7}\text{Na}_{0.3}\text{NbO}_3$ thin film does not depend on the sample temperature. Thus, we interpret the relative diffracted intensity from M_c - and c -domains as a *direct measure* of the volume fraction of the respective structural phase. In contrast, to the diffracted intensity, the lateral spacing Δq_{ds} of M_c -domain reflections changes abruptly at a temperature of 100°C (see supplemental material).

Since intensity mapping in reciprocal space provides important insights into the nature of temperature-driven phase transitions, we need to discuss it in more detail: Firstly, the redistribution of diffraction efficiency [cf. Fig. 1f, blue diamonds and red bullets] indicates a gradual transformation of the entire sample volume. Secondly, from the temperature dependence of Δq_{ds} , we observe an abrupt change of the structural symmetry from monoclinic to orthorhombic. Thus, Δq_{ds} denotes the structural order parameter of the phase transition. In combination, these are exemplary indicators of a first order phase transition. Specifically, this means that in a temperature range between $\approx 0^\circ\text{C}$ and $\approx 100^\circ\text{C}$ both the low temperature M_c - and the high temperature c -phase coexist. In consequence, the sample contains interfaces between different spatially separated structural phases that contribute to the total free energy of the system.

In the following paragraphs, we study the dynamics of the thermally driven phase transition. We use optical pulses with a duration of 7 ns at a wavelength of 1064 nm to excite the sample and monitor structural changes by measuring RSMs at different pump-probe delays. Note that the laser is not absorbed in the $\text{K}_{0.7}\text{Na}_{0.3}\text{NbO}_3$ film directly but in the SrRuO_3 bottom electrode. Due to the strong thermal coupling the temperature of both films equilibrate within the duration of the excitation pulse [44]. Details of the measurements that were performed at the synchrotron beamline P23 at Petra III/DESY are given in the Experimental

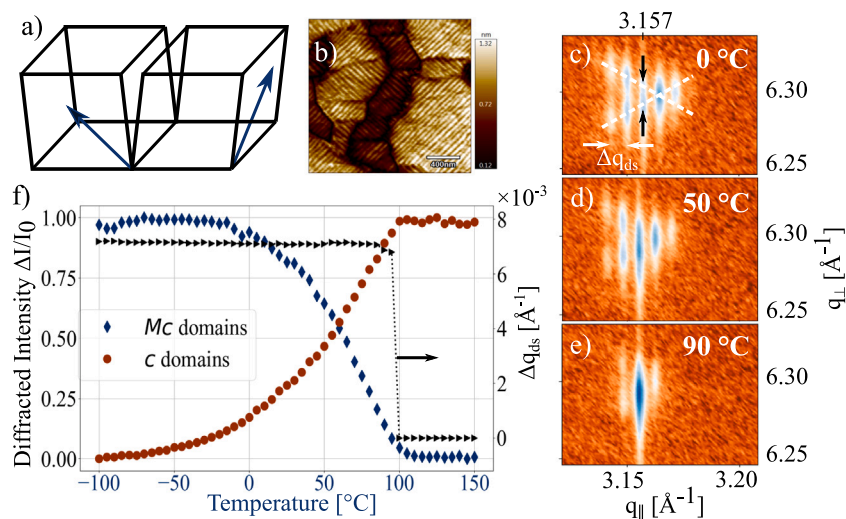


Fig. 1. Equilibrium characterization of $K_{0.7}Na_{0.3}NbO_3$: (a) Schematic of tilted M_c -domains. (b) Vertical Piezoresponse Force Microscopy (PFM) depicting the hierarchical order of nanometer-sized stripe- and micrometer-sized superdomains. (c) X-ray Reciprocal Space Map (RSM) in the q_x - q_y -plane measured at a sample temperature of 0 °C depicting features of tilted M_c -domains (vertical stripes) and superdomains (diagonal branches). The domain size of 45 nm can be retrieved from the lateral spacing Δq_{ds} of the domain peaks. The white dashed lines depict two branches of superdomains and the black arrows highlight the splitting along q_x that stems from the monoclinic tilt of the unit cell (see main text). (d) and (e) RSMs similar to (c) but depicting weaker diffraction from M_c -domains and stronger diffraction from c-domains, respectively, at higher sample temperatures. (f) Normalized temperature-dependent diffracted intensity from M_c - and c-domains (blue diamonds and red bullets, left vertical axis). The black triangles depict the temperature dependence of the average lateral spacing between domain peaks Δq_{ds} (right vertical axis). The data is exemplary for a first-order phase transition (see text for details).

Methods Section 4. To analyze our data we simulated the transient heating of the sample after absorption of the laser pulse by solving the heat diffusion equation using the `udkm1Dsim` - package [45]. In particular, the simulations allow to determine the temperature rise per absorbed fluence to ≈ 3.9 K/mJ/cm² in the $K_{0.7}Na_{0.3}NbO_3$ film.

Similar to the static heating, a transient temperature increase redistributes the diffraction efficiency from M_c - to c-domains. As an example, we depict a projection of the reciprocal space volume on the q_x - q_y -plane in the vicinity of the (620) reflection in Fig. 2(a)–(c) at pump-probe delays of –20 ns, 10 ns and 150 ns, respectively. The central peak denotes the orthorhombic c-phase and the off-center satellites stem from the periodically ordered domain boundaries of the M_c -phase. The data was recorded with an excitation fluence of 150 mJ/cm². The representative RSMs at different pump-probe delays show that the diffracted intensity from M_c domains is reduced upon excitation with the laser pulse and partly restored after 150 ns. The full evolution of the diffracted intensity in all M_c reflections is depicted in the orange line in Fig. 2(d). We observe a decrease of the transient diffracted intensity by 70%, as marked by the gray arrow in Fig. 2(d). In addition, we depict an exemplary simulation of the temperature evolution in the $K_{0.7}Na_{0.3}NbO_3$ film (black dashed line, right vertical axis).

Based on our previous analysis [cf. Fig. 1] the diffracted intensity is a measure for the corresponding volume fraction of the sample. We performed time-resolved diffraction measurements with excitation fluences from 13 mJ/cm² to 150 mJ/cm² and extract the maximum intensity change due to the laser heating. Results are marked as orange crosses in Fig. 2(e) together with the measured M_c -domain volume fraction from temperature-dependent RSM measurements (light blue squares) already depicted in Fig. 1(f). We interpret the relative intensity change $\Delta I(\tau)/I_0$ [cf. Fig. 2(d)] as M_c volume fraction in Fig. 2(e), where the gray arrow points out that both quantities are in fact exchangeable. The transformation of $\Delta I(\tau)/I_0$ to M_c volume fraction for all excitation fluences is shown in the supplement material.

Note that the static (lower x-axis) and transient (upper x-axis) temperature axis scale with a factor of ≈ 4.8 over the whole temperature range. Thus, in order to fully transform the sample into the high-temperature c phase, it must be heated to 480 °C by the 7 ns laser pulse instead of only 100 °C during static heating. For a detailed discussion of the speed of martensitic transformation and its energy dependence,

we would like to refer the reader to our recent work that is published elsewhere [46]. Here, we only like to point out that the dynamics of the phase transition, i.e., the transient redistribution of M_c - and c-phase, depends on the temperature gradient in the sample that is induced by the optical excitation [46–48]. An interesting result of our measurement is that the temperature scaling factor is independent of the excitation fluence and thus holds over a large range of different thermal gradients.

So far, we have studied the dynamics of the M_c - to c-phase transformation by monitoring the transient intensity of the short range stripe domain order via time-resolved RSM. Unfortunately, the measurements shown in Fig. 2 cannot resolve the formation of superdomains on μ m lengthscales due to insufficient spatial resolution. For that, we resort to scanning imaging diffraction experiments at the synchrotron beamline ID01 at the European Synchrotron ESRF. The instrument offers an X-ray beam that is focused to a diameter of 200 nm, i.e., larger than the 45 nm period of a stripe domain but smaller than the μ m-sized superdomains. Note, that adjacent superdomains of type 0°/180° and 90°/270° can be distinguished by differently oriented monoclinic stripe domains. We exploit this fact to image the superdomain distribution in the $K_{0.7}Na_{0.3}NbO_3$ film via scanning imaging XRD experiments. In a first step, we monitor the distribution of superdomains in the sample ex-situ after illumination with nanosecond laser pulses of different fluences. In a second step, we perform an in-situ space and time resolved pump-probe experiment to resolve the spatiotemporal dynamics of the superdomain formation.

For the ex-situ mapping of superdomains we scan the focused X-ray beam over a $100 \times 100 \mu\text{m}^2$ area of the sample with 500 nm steps. At every spatial position we measure an RSM to detect the presence of M_c - or c-domains. The orientation of M_c -domains, which is specific to a superdomain, is also resolved by the RSM.

Exemplary results of these measurements for a fluence of 55, 65 and 115 mJ/cm² are depicted in Fig. 3(a)–(c), respectively. To detect laser-induced changes in the domain pattern, we first map the domain distribution before laser exposure [left images in Fig. 3(a)–(c)], second illuminate the sample with the pulsed laser for one minute and third scan the same area of the sample again to detect changes in the domain pattern [middle images in Fig. 3(a)–(c)]. All images are normalized to the maximum intensity in the scanning area. We employ the *structural image similarity index* (SISI) [49] to quantify laser-induced changes of

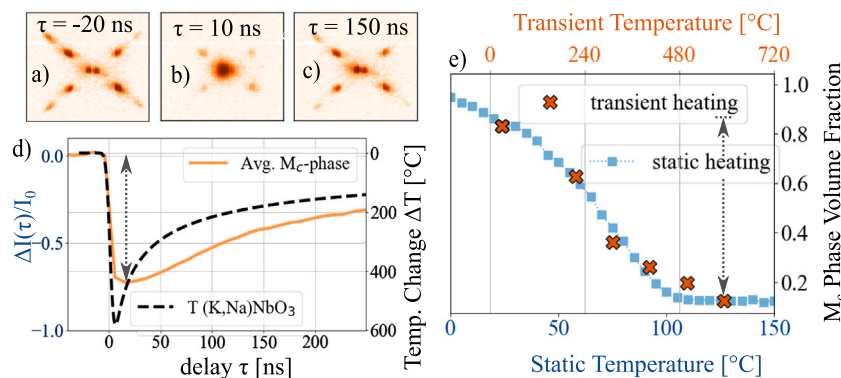


Fig. 2. Dynamic characterization of $K_{0.7}Na_{0.3}NbO_3$: (a)–(c) RSM (q_x - q_y plane) recorded at a pump-probe delay of -20 ns, 10 ns and 150 ns. (d) Relative transient diffracted intensity from M_c -domains (orange line). The black dashed line depicts the simulated transient temperature change in the sample. (e) Fraction of M_c -domains of the sample volume as a function of static (lower axis, blue squares) and transient (upper axis, orange crosses) temperature.

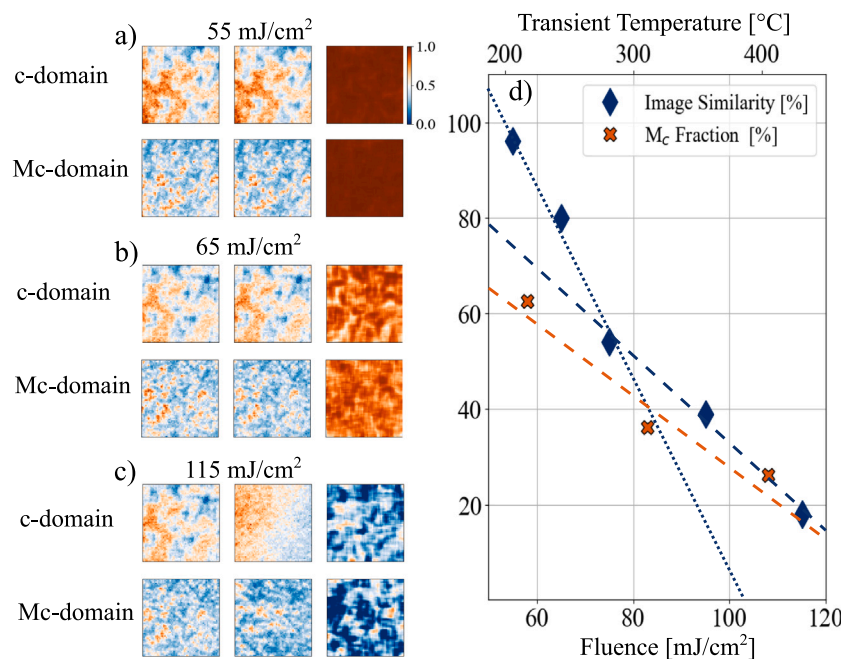


Fig. 3. Image Similarity $K_{0.7}Na_{0.3}NbO_3$: (a)–(c) Ex-situ normalized intensity maps of c - and M_c -domains, respectively, before (left) and after (middle) laser illumination. The field of view is $(100 \times 100) \mu\text{m}^2$ measured on a 500 nm spatial grid with 200 nm resolution of the focused X-ray beam. The right panels show the comparison (SISI) of both maps. The colorbar for all maps is shown in the first row. The pulsed laser impinges the sample for 1 min with a fluence of 55 , 65 and 115 mJ/cm^2 . (d) Image similarity (blue diamonds, see main text for details) and M_c volume fraction (orange crosses) vs. laser fluence. The dashed and dotted lines are guides to the eye.

the domain pattern. The similarity map is shown in the right image in Fig. 3(a)–(c) and is a measure of the similarity of the domain morphology before and after laser illumination. The upper and lower row in Fig. 3(a)–(c) depict the distribution of c - and M_c (one orientation only) domains, respectively. For a laser fluence of 55 mJ/cm^2 and 65 mJ/cm^2 the domain morphology is quite stable (see Fig. 3(a) and (b), respectively), but changes drastically at higher fluences.

To compare laser-induced changes in the superdomain distribution at different excitation strength, we depict the total integrated SISI (Image Similarity) vs. the laser fluence in Fig. 3(d). This quantity is the average of the area integrals of the SISI of all four M_c stripe domain orientations. For a fluence below 65 mJ/cm^2 the domain morphology is at least 80% similar to the initial distribution. The similarity decays for higher fluences. It is instructive to compare the Image Similarity to the laser-induced change of the M_c -domain volume fraction from Fig. 2(e) (orange crosses). The former quantifies changes to the domain morphology while the latter denotes the fraction of the probed sample volume that undergoes a phase transition upon exposure to a laser pulse.

Illumination of the sample with a fluence of 60 mJ/cm^2 leaves the M_c -domain morphology 80% unchanged. The time-resolved measurement at the same fluence reveals that the sample volume in the M_c phase is transiently reduced to almost 60% . In fact, from the measured fluence dependence of the Image Similarity and M_c volume fraction we deduce that the M_c volume must reduce at least to $\approx 50\%$ of the sample volume to change the domain morphology by a comparable amount. This behavior is reflected in the slope of the image similarity, which is steeper for low fluences, as indicated by the dotted and dashed blue lines in Fig. 3(d). The dashed orange line is a guide to the eye for the fluence dependence of the transformed volume fraction. The slopes of the dashed lines are comparable.

To better understand the interplay of phase transformation and domain morphology, we performed scanning imaging XRD measurements in time-resolved mode. The main implication of this mode for the measurement is a significant reduction of the X-ray flux due to the low repetition rate of the laser of 1 kHz [50]. To limit the data acquisition time to a reasonable amount, we reduced the scanning area to $(10 \times 10) \mu\text{m}^2$ and kept the spatial resolution. Again, we measure

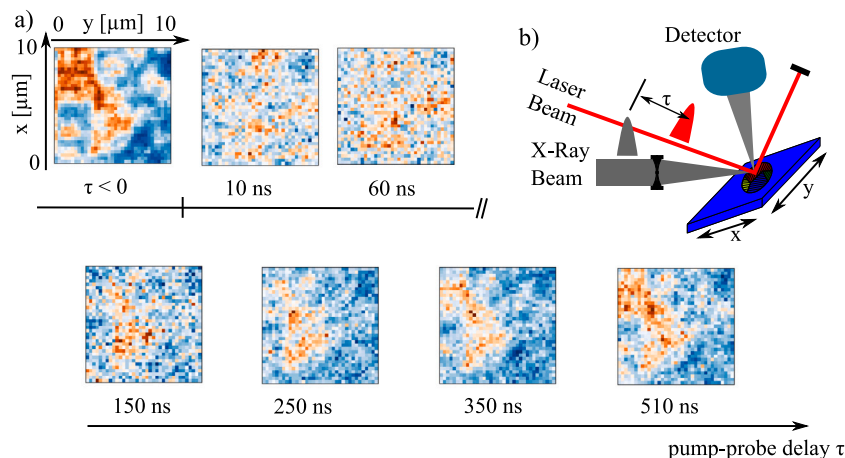


Fig. 4. Hierarchical transient ordering in $K_{0.7}Na_{0.3}NbO_3$: (a) Normalized intensity maps of one M_c -domain orientation at different pump-probe delays for a laser fluence of 65 mJ/cm^2 . The field of view is $(10 \times 10) \mu\text{m}^2$ with a spatial grid and resolution of 500 nm and 200 nm, respectively. (b) Sketch of the time- and space-resolved scanning imaging XRD measurement performed at ID01, ESRF.

RSMs at every point of the spatial grid. With these settings, measuring a full map at a single pump-probe delay took about 10 h, enough time to measure a total of 6 delay points.

For the time-dependent measurements we choose an excitation fluence of 65 mJ/cm^2 . From Fig. 3(d) we expect an 80% different domain distribution even though the absorbed laser pulse reduces the transient volume fraction of the M_c -phase to 60%. Maps of an M_c -domain orientation at different pump-probe delays are shown in Fig. 4(a) and the time- and space-resolved scanning XRD measurement which stretches diagonally from the upper left corner of the images. The first delay point ($\tau < 0$) was measured in static mode at high X-ray flux to save beamtime. Comparison to the other spatial maps reveals the lower signal-to-noise-ratio (SNR) of the time-resolved mode, which has to be accounted for in the interpretation of the data. The transient data depict a melting of the initial superdomain upon laser excitation and subsequent condensation into a similar spatial pattern within several hundred nanoseconds. We like to emphasize the data acquisition time of a single 2D map at each delay point of $\approx 10 \text{ h}$, which underlines the stability of the domain morphology under constant laser illumination.

We now interpret the spatiotemporal phase transition dynamics observed in Figs. 2 to 4. The discrepancy of stability of the domain distribution and M_c - to c -phase transformation at a fluence of 60 – 80 mJ/cm^2 points to a self-stabilizing mechanism of the ferroelectric equilibrium state. Note that the conservation of 90° domain walls in $(K,Na)NbO_3$ has already been observed during cooling from the tetragonal to the orthorhombic phase [51]. Our results in thin $(K,Na)NbO_3$ films indicate an energy threshold for the alteration of the domain morphology. In other words, M_c -domains that undergo a phase transition are likely to condense into a previous superdomain upon cooling. This behavior is evident from the slope of the dotted line in Fig. 3(d), which has a different fluence dependence than the M_c volume fraction. Nevertheless, the long-range order within a superdomain melts even at these comparably low fluences. The superdomain recovers its previous shape upon cooling within few hundred nanoseconds. At stronger excitations ($>80 \text{ mJ/cm}^2$), the domain distribution and M_c volume fraction have a similar fluence dependence [cf. dashed lines in Fig. 3(d)]. We have high confidence in the validity of our data due to the continuous exposure of the sample to the laser beam and the nevertheless observed stability of the domain morphology at a fluence of 65 mJ/cm^2 .

From the various domain formation mechanisms discussed in literature [4,6,7,21–28] our repetitive fast thermal cycling experiment favors processes which involve nucleation at structural defects. These sites pin an existing domain morphology, thus favoring condensation of the low temperature phase in the original pattern. In order to

generate a different morphology, the system requires a disproportionately higher energy. An alternative explanation could involve charged domain boundaries which have also been reported to stabilize the domain morphology [52]. Ultimately, further studies will be necessary to ascertain the mechanism of domain formation in $(K,Na)NbO_3$ and comparable materials. This should include a mapping of the local FE polarization, which was not performed in our study.

3. Conclusion

In summary, we have employed a combination of time-resolved X-ray diffraction and scanning X-ray microscopy to investigate the local domain formation dynamics at high spatial and temporal resolution. We investigate 50 nm thin films of ferroelectric $K_{0.7}Na_{0.3}NbO_3$, which display a rich hierarchical order of domains and superdomains in the low temperature M_c -phase. We discovered a self-stabilization mechanism which conserves an existing domain morphology during thermal cycling across the phase transition.

$K_{0.7}Na_{0.3}NbO_3$ is a promising candidate to replace lead-based solid solutions in ferro- and piezoelectric applications for energy conversion such as electrocalorics and energy harvesting but also in mobile communication or in sensor technology. However, the spatiotemporal correlation of the domain morphology during a thermal cycle will affect the change in entropy across the phase transition and thus the energy conversion efficiency [38,39,53]. Such applications rely on the application of external stimuli like current, voltage or light pulses, which induce a non-equilibrium state in the system. The self-stabilization corresponds to an additional fraction of the total free energy of the solid.

4. Experimental section

4.1. Sample growth

The $K_{0.7}Na_{0.3}NbO_3$ film was epitaxially grown on 0.1° off-oriented (110) $TbScO_3$ substrates by liquid-delivery spin metal–organic vapor phase epitaxy (MOVPE). MOVPE is a chemical deposition method which works close to thermodynamic equilibrium and at elevated oxygen partial pressure, thus providing films with high structural perfection and highly regular domain formation. Epitaxial growth was performed at a substrate temperature of 700°C and a gas pressure of $2.6 \times 10^3 \text{ Pa}$ with an argon to oxygen ratio of 1.6. Further details of the deposition process are described elsewhere [15]. The $SrRuO_3$ bottom electrode with a thickness of 20 nm was grown fully strained by pulsed laser deposition at a substrate temperature of 750°C in oxygen pressure of 0.05 mbar. A KrF laser was used with a frequency of 5 Hz and a fluence of 2 mJ/cm^2 .

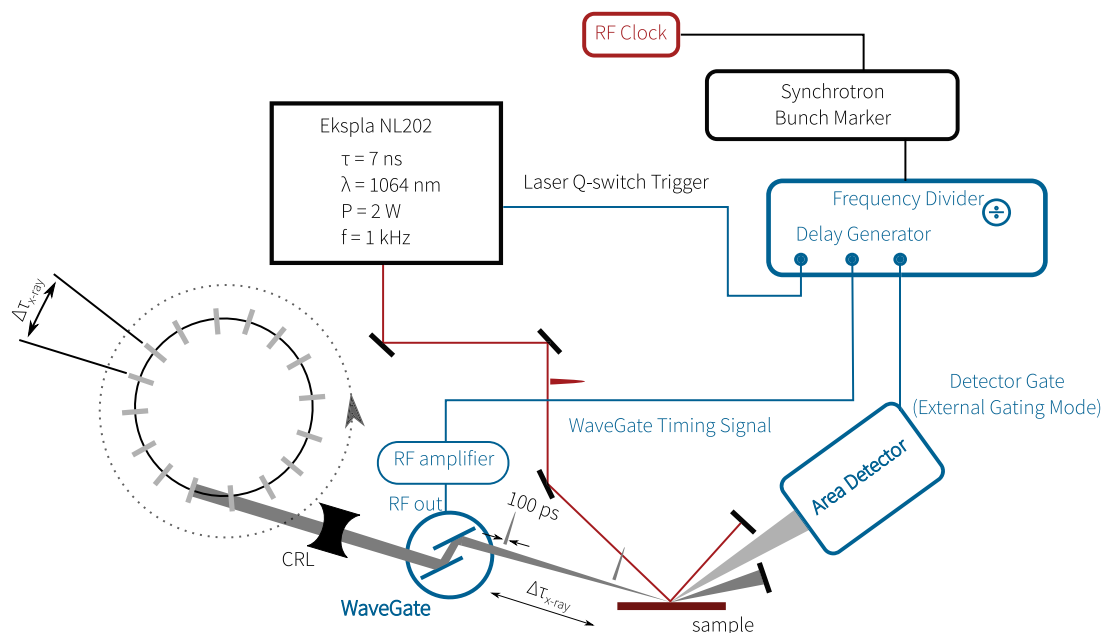


Fig. 5. Time-resolved X-ray diffraction setup: An Ekspla NL202 q-switch laser is synchronized to the storage ring via a bunch marker signal. Timing signals for the laser, the detector and for the WaveGate Pulse Picker (only at the DESY/Petra III beamline P23) were generated at a repetition rate of 1 kHz. The sample was mounted on a goniometer and diffracted photons are captured on a area detector which was used in external gating mode. Details specific to the setups at P23/DESY and ID01/ESRF are given in the main text.

4.2. Time-resolved X-ray diffraction measurements

The synchrotron experiments were performed at beamlines P23 at the storage ring Petra III/DESY and ID01 at the European Synchrotron ESRF. The experimental setup is sketched in Fig. 5. In both experiments we employ the same nanosecond laser (Ekspla NL202) with pulse duration, wavelength, pulse repetition rate and average output power of 7 ns, 1064 nm, 1 kHz and 2 W, respectively. In both experiments we determined the laser footprint on the sample in a knife-edge measurement to convert the laser power to an excitation fluence. The laser is synchronized via a bunch marker signal provided by the storage ring, that is fed into a frequency divider. A subsequent delay generator (Stanford Research DG645) generates all timing signals for the laser, the detector gate and for the WaveGate X-ray pulse picker (TXproducts UG).

The X-ray photon energy at beamline P23 was 9.1 keV. The beam was moderately focused to a spot size of $(30 \times 160) \mu\text{m}^2$ by a set of Be compound refracting lenses located ≈ 30 m upstream from the sample position. We employed a Lambda 100k area detector (XSpec-tum GmbH) in external enable mode. Reciprocal Space Maps (RSMs) were recorded by scanning the incidence and diffraction angles of the sample on a 5 + 2 circle diffractometer (Huber GmbH). The sample was mounted on a furnace (Anton Paar ProveTec GmbH) to control the base temperature.

The time-resolved scanning X-ray diffraction microscopy measurements were performed at beamline ID01/ESRF [54]. The X-ray photon energy was set to 9 keV and the beam was focused to a round spot with a diameter of 200 μm using compound refractive lenses. For the spatial scans, the sample was moved with a stepsize of 500 nm in both lateral directions using a PI-Mars three-axis piezo stage. We employed an Eiger detector ($75 \mu\text{m} \times 75 \mu\text{m}$ pixels, 1030×2164) which was mounted on the detector arm rotating in the vertical plane.

CRedit authorship contribution statement

Peter Gaal: Conceived the experiment, Funding acquisition, Performed measurements, Performed data analysis, Writing – original draft, review and editing. **Daniel Schmidt:** Performed measurements,

review and editing. **Mallika Khosla:** Performed measurements, data analysis, review and editing. **Carsten Richter:** Performed measurements, data analysis, review and editing. **Peter Boesecke:** Performed measurements, review and editing. **Dmitri Novikov:** Performed measurements, review and editing. **Martin Schmidbauer:** Performed measurements, review and editing. **Jutta Schwarzkopf:** Funding acquisition, samples growth and preparation, review and editing.

Declaration of competing interest

The authors declare that they have no known competing financial interests or personal relationships that could have appeared to influence the work reported in this paper.

Data availability

Not all raw/processed data required to reproduce these findings can be shared at this time due to technical or time limitations. Data measured at ID01/ESRF is accessible via DOI <https://doi.org/10.15151/ESRF-ES-594730606>. All other data is available from the authors upon reasonable request.

Acknowledgments

We acknowledge financial support by Deutsche Forschungsgemeinschaft, Germany via grant GA 2558/5-1 and FE 1438/2-1 as well as European Regional Development Fund (ERDF) (Project No. 1.8/15). This work was performed in the framework of GraFOX, a Leibniz ScienceCampus. We acknowledge DESY (Hamburg, Germany), a member of the Helmholtz Association HGF, for the provision of experimental facilities. Parts of this research were carried out at Petra III and we would like to thank Azat Khadiev and Yury Matveev for assistance in using beamline P23. Beamtime was allocated for proposal I-20210573 and I-20190850. We acknowledge the European Synchrotron Radiation Facility (ESRF) for provision of synchrotron radiation facilities and we would like to thank Steven Leake for assistance and support in using beamline ID01. Data is accessible via DOI 10.15151/ESRF-ES-594730606. We are grateful to Roman Bauer and Benedickt Kubicki for support during the synchrotron measurements. All authors contributed to discussions and to the final version of the manuscript.

Data availability statement

Not all raw/processed data required to reproduce these findings can be shared at this time due to technical or time limitations. Data measured at ID01/ESRF is accessible via DOI 10.15151/ESRF-ES-594730606. All other data is available from the authors upon reasonable request.

Appendix A. Supplementary data

Supplementary material related to this article can be found online at <https://doi.org/10.1016/j.apsusc.2022.155891>.

References

- [1] T. Mitsui, J. Furuichi, *Phys. Rev.* 90 (1953) 193.
- [2] E.K.W. Goo, R.K. Mishra, G. Thomas, *J. Appl. Phys.* 52 (4) (1981) 2940.
- [3] J. Ricote, R.W. Whatmore, D.J. Barber, *J. Phys.: Condens. Matter* 12 (3) (1999) 323.
- [4] W.J. Merz, *Phys. Rev.* 95 (1954) 690.
- [5] V. Zhirmov, *Sov. Phys. JEPT* 6 (1959) 1175.
- [6] M. Paściak, S.E. Boulfelfel, S. Leoni, *J. Phys. Chem. B* 114 (49) (2010) 16465.
- [7] J. Li, L. Zhong, R. Jangid, Meera, G. Rippey, K. Ainslie, C. Kohne, A.S. Everhardt, B. Noheda, Y. Zhang, A. Fluerasu, S. Matzen, R. Kukreja, *Phys. Rev. Mater.* 4 (2020) 114409.
- [8] C. Kittel, *Phys. Rev.* 70 (1946) 965.
- [9] L. Bulaeewski, *Sov. Phys.—Solid State* 5 (1964) 2329.
- [10] B. Meyer, D. Vanderbilt, *Phys. Rev. B* 65 (2002) 104111.
- [11] G. Arlt, *J. Mater. Sci.* 25 (6) (1990) 2655.
- [12] J. Erhart, W. Cao, *J. Appl. Phys.* 94 (5) (2003) 3436.
- [13] K.J. Choi, M. Biegalski, Y.L. Li, A. Sharan, J. Schubert, R. Uecker, P. Reiche, Y.B. Chen, X.Q. Pan, V. Gopalan, L.-Q. Chen, D.G. Schlom, C.B. Eom, *Science* 306 (5698) (2004) 1005.
- [14] D.G. Schlom, L.-Q. Chen, C.-B. Eom, K.M. Rabe, S.K. Streiffer, J.-M. Triscone, *Annu. Rev. Mater. Res.* 37 (26) (2007) 1589.
- [15] J. Schwarzkopf, D. Braun, M. Hanke, R. Uecker, M. Schmidbauer, *Front. Mater.* 4 (2017).
- [16] G.F. Nataf, M. Guennou, J.M. Gregg, D. Meier, J. Hlinka, E.K.H. Salje, J. Kreisel, *Nat. Rev. Phys.* 2 (11) (2020) 634.
- [17] L.D. Landau, E. Lifschitz, Berlin Akademie Verlag, 1975, 978-3817113262.
- [18] K. Rabe, C. Ahn, J. Triscone, Berlin:Springer, 2007, http://dx.doi.org/10.1007/978-3-540-34591-6_1.
- [19] B. Noheda, D.E. Cox, G. Shirane, J.A. Gonzalo, L.E. Cross, S.-E. Park, *Appl. Phys. Lett.* 74 (14) (1999) 2059.
- [20] L.A. Schmitt, K.A. Schönau, R. Theissmann, H. Fuess, H. Kungl, M.J. Hoffmann, *J. Appl. Phys.* 101 (7) (2007) 074107.
- [21] J.E. Daniels, C. Cozzan, S. Ukritnukun, G. Tutuncu, J. Andrieux, J. Glaum, C. Dosch, W. Jo, J.L. Jones, *J. Appl. Phys.* 115 (22) (2014) 224104.
- [22] Y.A. Genenko, R. Khachatryan, J. Schultheiß, A. Ossipov, J.E. Daniels, J. Koruza, *Phys. Rev. B* 97 (2018) 144101.
- [23] Y. Xu, D. Xue, Y. Zhou, T. Su, X. Ding, J. Sun, E.K.H. Salje, *Appl. Phys. Lett.* 115 (2) (2019) 022901.
- [24] N.A. Tikhomirova, S.A. Pikin, L.A. Shuvalov, L.I. Dontsova, E.S. Popov, A.V. Shilnikov, L.G. Bulatova, *Ferroelectrics* 29 (1) (1980) 145.
- [25] Z.-G. Ye, M. Dong, *J. Appl. Phys.* 87 (5) (2000) 2312.
- [26] T. Limboeck, E. Soergel, *Appl. Phys. Lett.* 105 (15) (2014) 152901.
- [27] J. Döring, L.M. Eng, S.C. Kehr, *J. Appl. Phys.* 120 (8) (2016) 084103.
- [28] A. Grünebohm, M. Marathe, *Phys. Rev. Mater.* 4 (2020) 114417.
- [29] W.J. Kuhn, *Ferroelectr. Lett. Sect.* 13 (5) (1991) 101.
- [30] A. Grünebohm, M. Marathe, R. Khachatryan, R. Schiedung, D.C. Lupascu, V.V. Shvartsman, *J. Phys.: Condens. Matter* 34 (7) (2021) 073002.
- [31] T. Danz, T. Domröse, C. Ropers, *Science* 371 (6527) (2021) 371.
- [32] H. Wen, M.J. Cherukara, M.V. Holt, *Annu. Rev. Mater. Res.* 49 (1) (2019) 389.
- [33] J. Rödel, W. Jo, K.T.P. Seifert, E.-M. Anton, T. Granzow, D. Damjanovic, *J. Am. Ceram. Soc.* 92 (6) (2009) 1153.
- [34] T.T. Lummen, Y. Gu, J. Wang, S. Lei, F. Xue, A. Kumar, A.T. Barnes, E. Barnes, S. Denev, A. Belianinov, M. Holt, A.N. Morozovska, S.V. Kalinin, L.-Q. Chen, V. Gopalan, *Nature Commun.* 5 (1) (2014) 3172.
- [35] A.L. Roytburd, J. Ouyang, A. Artemev, *J. Phys.: Condens. Matter* 29 (16) (2017) 163001.
- [36] P. Sharma, R.G.P. McQuaid, L.J. McGilly, J.M. Gregg, A. Gruverman, *Adv. Mater.* 25 (9) (2013) 1323.
- [37] S. Schwabe, R. Niemann, A. Backen, D. Wolf, C. Damm, T. Walter, H. Seiner, O. Hezcko, K. Nielsch, S. Fähler, *Adv. Funct. Mater.* 31 (7) (2021) 2005715.
- [38] X. Moya, S. Kar-Narayan, N.D. Mathur, *Nature Mater.* 13 (5) (2014) 439.
- [39] N. Sezer, M. Koç, *Nano Energy* 80 (2021) 105567.
- [40] L. von Helden, L. Bogula, P.-E. Janolin, M. Hanke, T. Breuer, M. Schmidbauer, S. Ganschow, J. Schwarzkopf, *Appl. Phys. Lett.* 114 (23) (2019) 232905.
- [41] L. von Helden, M. Schmidbauer, S. Liang, M. Hanke, R. Wördenweber, J. Schwarzkopf, *Nanotechnology* 29 (41) (2018) 415704.
- [42] B. Veličkov, V. Kahlenberg, R. Bertram, R. Uecker, *Acta Crystallogr. Sect. E* 64 (11) (2008) i79.
- [43] A. Vaillonis, H. Boschker, W. Siemons, E.P. Houwman, D.H.A. Blank, G. Rijnders, G. Koster, *Phys. Rev. B* 83 (2011) 064101.
- [44] See supplemental material.
- [45] D. Schick, *Comput. Phys. Comm.* 266 (2021) 108031.
- [46] S. Schwabe, K. Lünser, D. Schmidt, K. Nielsch, P. Gaal, S. Fähler, What is the speed limit of martensitic transformations? *Sci. Technol. Adv. Mater.* (2022) (in print).
- [47] E.K.H. Salje, S.A. Hayward, W.T. Lee, *Acta Crystallogr. Sect. A* 61 (1) (2005) 3.
- [48] K. Binder, *Phys. Rev. B* 8 (1973) 3423.
- [49] R. Dosselmann, X.D. Yang, *Signal, Image Video Process.* 5 (1) (2011) 81.
- [50] R. Shayduk, D. Pennicard, K. Krausert, P. Gaal, S. Volkov, V. Vonk, U. Hejral, M. Jankowski, M. Reinhardt, W. Leitenberger, A. Stierle, *J. Synchrotron Radiat.* 24 (5) (2017) 1082.
- [51] X.R. Huang, S.S. Jiang, X.Y. Xu, J.Y. Wang, Q.C. Guan, J.H. Jiang, D. Feng, *Phys. Status Solidi (A)* 148 (2) (1995) 611.
- [52] S. Xiao, Y. Jin, X. Lu, S.-W. Cheong, J. Li, Y. Li, F. Huang, J. Zhu, *Nat. Sci. Rev.* 7 (2) (2019) 278.
- [53] Z.-K. Liu, *Mater. Res. Lett.* 10 (7) (2022) 393.
- [54] S.J. Leake, G.A. Chahine, H. Djazouli, T. Zhou, C. Richter, J. Hilhorst, L. Petit, M.-I. Richard, C. Morawe, R. Barrett, L. Zhang, R.A. Homs-Regajo, V. Favre-Nicolin, P. Boescke, T.U. Schüll, *J. Synchrotron Radiat.* 26 (2) (2019) 571.